Article

Optimization of ^{99m}Tc-MAA SPECT/CT Imaging for ^{90}Y Radioembolization Using a 3D-Printed Phantom

Sara Ungania [1], Marco D'Arienzo [2,*], Sandro Nocentini [1], Marco D'Andrea [1], Vicente Bruzzaniti [1], Raffaella Marconi [1], Emilio Mezzenga [3], Bartolomeo Cassano [1], Erminia Infusino [1], Antonino Guerrisi [4], Antonella Soriani [1] and Lidia Strigari [5]

1. Laboratory of Medical Physics and Expert Systems, IRCCS Regina Elena National Cancer Institute, 00144 Rome, Italy
2. Medical Physics, ASL Roma 6, UOSD Fisica Sanitaria, Ospedale dei Castelli, Ariccia, 00040 Rome, Italy
3. Medical Physics Unit, IRCCS Istituto Romagnolo per lo Studio dei Tumori (IRST) "Dino Amadori", 47014 Meldola, Italy
4. Radiology Department, IRCCS Regina Elena National Cancer Institute, 00144 Rome, Italy
5. Department of Medical Physics, IRCCS Azienda Ospedaliero-Universitaria di Bologna, 40138 Bologna, Italy
* Correspondence: marco.darienzo@aslroma6.it

Abstract: Radioembolization (RE) with ^{90}Y-microspheres has gained widespread acceptance as a safe and effective technique for treating liver malignancies. Accurate quantification in RE is a key step in treatment planning optimization and is becoming a pressing issue in light of the Directive 2013/59/EURATOM. The aim of this study was to develop a SPECT/CT imaging protocol for quantitative imaging optimization in RE based on cutting edge imaging technology (Symbia IntevoTM system provided with the innovative xSPECT software) and a novel anthropomorphic 3D-printed phantom. In the present study, ^{99m}Tc-labeled macroaggregated albumin was used as a surrogate radiopharmaceutical for treatment planning. Gamma camera calibration factors and recovery coefficients were determined performing preliminary SPECT/CT acquisitions of a point source, a cylindrical homogeneous phantom and the NEMA/IEC phantom. Data reconstruction was performed using the built-in xSPECT package, using both the Ordered Subset Expectation–Maximization (OSEM) and the Ordered Subset Conjugated Gradient (OSCG) algorithm. Specific regions of interest (ROIs) were drawn on the MIM 6.1.7 system according to the physical volume. The quantification procedure was validated using the anthropomorphic phantom provided with a fillable liver section and spheres of different diameters (20 mm, 40 mm and a 40 mm spherical shell). The measured activity concentration in all geometries is consistent within 4%, demonstrating that the xSPECT software permit an absolute quantification in anthropomorphic geometry largely within the 10% recommended from the manufacturer. Caution is advised in the presence of spherical objects with a necrotic core, as underestimations in the order of 20% were obtained.

Keywords: molecular radiotherapy; diagnostic imaging; radioembolization; data reconstruction; quantitative imaging

1. Introduction

Primary liver cancer is the sixth most commonly diagnosed cancer and the third leading cause of cancer death world-wide in 2020, with approximately 906,000 new cases and 830,000 [1]. Rates of both incidence and mortality are 2 to 3 times higher among men than among women in most regions and liver cancer ranks fifth in terms of global incidence and second in terms of mortality for men [1]. The global estimated average incidence to mortality ratio is 1.07 for men and 1.06 for women [2] and the disease burden attributable to this cancer induces a substantial number of years of life lost [3]. Consequently, due to its extremely aggressive nature and poor survival rate [4], it represents an important public health issue worldwide.

The management of this disease is determined after stratification into three groups: (I) resectable; (II) unresectable or medically inoperable; and (III) metastatic. Unfortunately, the majority (50–90%) of liver cancer patients present with unresectable disease [5,6]. In these situations, multimodality management with a combination of radiation oncology, medical oncology, surgical oncology, and interventional radiology is crucial.

Over the last years, therapy with ^{90}Y-labeled microspheres has gained widespread acceptance as a safe and effective technique for treating hepatocellular carcinoma (HCC) and metastatic liver malignancies with a growing number of ongoing trials. This therapeutic option is also known as radioembolization (RE). During RE ^{90}Y-laden microspheres are injected directly within the tumor through the hepatic artery and become trapped at the precapillary level delivering a potentially tumoricidal dose to the target tumor while sparing surrounding normal parenchyma, thereby permitting a selective delivery of the microspheres [7,8].

^{99m}Tc-labeled macroaggregated albumin (^{99m}Tc-MAA) has been largely used as a surrogate radiopharmaceutical for treatment planning. The underlying assumption is that ^{99m}Tc-MAA biodistribution simulates the expected microsphere delivery during ^{90}Y radioembolization. Since the inception of the therapy, planar imaging using ^{99m}Tc-MAA has been successfully used to assess the lung shunt fraction and to estimate the absorbed dose to lungs after ^{90}Y RE treatment. Of note, the assessment of extrahepatic shunting is particularly important in the case of primary disease, as lung shunting fraction exceeding 20% has been observed for HCC [9]. With the advent of hybrid SPECT/CT systems, ^{99m}Tc -MAA administration before therapy has begun to be used to obtain in vivo quantitative information on the estimated microsphere biodistribution following the therapeutic administration. Furthermore, when used in conjunction with dosimetry models, ^{99m}Tc-MAA biodistribution may provide estimated absorbed doses both to lesions and liver parenchyma. In fact, absorbed doses estimates can be mathematically determined by converting quantitative ^{99m}Tc-MAA SPECT data to the absolute ^{90}Y activity and then converting these values to absorbed doses estimates using the available dose calculation algorithms (e.g., MIRD [10], partition [11], kernel convolution [12,13] or local deposition models [12,13]). The consensus is that SPECT/CT-based dosimetry is superior to planar scintigraphy by tomographically resolving overlapping radiotracer activity, evaluating heterogeneous radiotracer uptake, and detecting activity in small lesions [14]. In addition, several phantom studies have shown that ^{99m}Tc-MAA SPECT/CT volume measurements are accurate and reproducible, although additional measurements on patient-like phantoms are needed [15,16].

Recent evidence suggests that the combination of anthropomorphic phantoms with quantitative software (such as xSPECT or Hermes SUV-SPECT software) could represent a major step forward in improving image accuracy and predictability of therapy planning [17]. It is generally acknowledged that quantitative calibration of the imaging system is one of the critical steps associated with in vivo activity assessment in nuclear medicine. Calibration of the imaging system consists in converting reconstructed voxel values to absolute activity or activity concentration. However, contrary to positron emission tomography (PET) that was developed as a quantitative tool SPECT has traditionally been considered as non-quantitative. This is because quantitative analysis using SPECT data is a time-consuming process requiring accurate algorithms and techniques that correct for several degrading factors, among which are attenuation, scatter, dead time, and partial volume effects. However, recent advances in image processing software and the advent of hybrid SPECT/CT systems have made quantitative SPECT viable in a manner similar to quantitative PET.

The aim of our research was to perform quantitative analysis of ^{99m}Tc-MAA scintigrafic imaging in a novel anthropomorphic set-up. Against this backdrop, we developed a workflow that relies on SPECT/CT data to assess the accuracy of quantitative analysis using a 3D-printed anthropomorphic phantom (Abdo-Man) provided with a number of spherical inserts contained in the liver volume. Recent work [15] has demonstrated that Abdo-Man can be successfully used for assessing the quantitative accuracy in RE using

different imaging modalities. The use of such a phantom, along with up-to-date technology and optimization acquisition protocols has the potential to improve outcome for patients.

2. Materials and Methods

In the present work all acquisitions were performed using a Symbia IntevoTM system (Siemens, Erlangen, Germany) provided with the novel xSPECT software, specifically dedicated to quantitative imaging. The software uses CT as the frame-of-reference for image reconstruction, preserving the resolution of the CT matrix and permitting a more accurate alignment of both data sets during reconstruction. The resulting reconstructed xSPECT image is created in a CT equivalent slice-by-slice DICOM format.

Since the photopeak of ^{99m}Tc is at 140 keV, low-energy high-resolution (LEHR) collimators were used for all phantoms. To simulate clinical conditions, images were acquired using the acquisition workflow currently adopted by our Institute for patients undergoing RE treatment, i.e., 256 × 256 matrix (2.39 mm^3 voxel size), angular step of 5° over 360° (75 frames) and a 15% energy window centered at 140 keV. Acquisitions were made with the phantoms in the center of the field of view. Raw data were corrected both for attenuation and scatter. Furthermore, data were decay corrected to the acquisition time.

The activities used for the preparation of the phantoms were measured in the Calibrator of Eliza hot-cell (COMECER S.p.a), traceable to the Italian National Institute of Ionizing Radiation Metrology for the geometry being measured (accuracy within ±5% at k = 2 level, as recommended by AAPM report 181 [18]).

The work is structured into four logically sequential steps, as follows:

(1) Assessment of gamma camera calibration factor using a NIST traceable ^{57}Co point source;
(2) Selection of reconstruction method: using the calibration factor derived from the previous step, data acquisition of a homogeneous cylindrical phantom was performed in order to assess the best reconstruction method. Two algorithms were tested (the OSEM and OSCG algorithm) using the built-in quantitative xSPECT package. The selected algorithm was then used to reconstruct raw data in step (3) and (4);
(3) Determination of recovery coefficient: acquisition of the NEMA-IEC phantom provided with 6 fillable spheres was carried out in order to assess recovery coefficients for small volumes;
(4) Method validation: using information elicited from the previous steps, the quantification procedure was validated using a 3D-printed anthropomorphic phantom provided with fillable spheres simulating hepatic lesions.

A summary of experimental materials and methods described in the present work is shown in Figure 1.
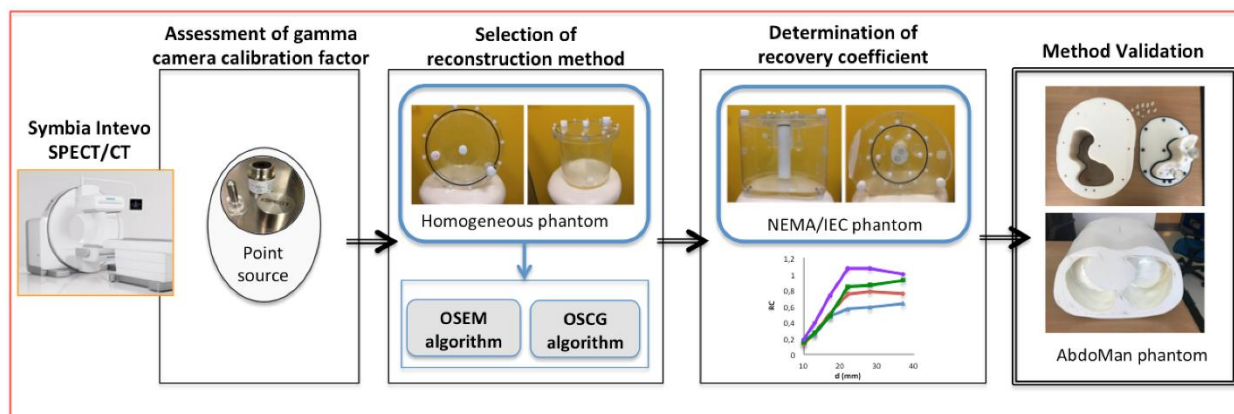

Figure 1. Experimental materials and methods described in the present work.

2.1. Assessment of Gamma Camera Calibration Factor

Gamma camera calibration factor was assessed using a 3% NIST traceable reference [57]Co point source (Table 1), routinely used in our institute for constancy test of the gamma camera sensitivity. In particular, the activity of the source was 114.7 MBq at the time of measurement. Planar acquisition of the point source placed in air was performed according to the calibration procedure of the system manual. Briefly, the built-in software of the SPECT/CT system automatically places a region of interest (ROI) corresponding to the entire field of view of the planar images and provides the nominal and measured sensitivity of each head.

Based on the average counts within the ROIs (i.e., counts), the calibration factor (F_{cal}) is automatically computed as follows:

$$F_{cal} = \frac{A_S}{counts} \tag{1}$$

i.e., the ratio of the known source activity A_S at the moment of the measure divided by the average counts calculated in the entire field of view [19].

Table 1. The main geometrical characteristics of the investigated phantoms/geometries.

Phantom	Nominal Volume (mL)	Length (cm)	Outside Diameter (cm)
Point-like source	0.1	0.01	0.01
Homogeneous cylindrical	6462	17	22
NEMA/IEC	9700	18	30
Abdo-Man	1783	25.1	34.2

2.2. Selection of Reconstruction Method Using a Cylindrical Phantom

Two reconstruction methods were compared using a cylindrical phantom filled with water uniformly mixed with radioactive ^{99m}Tc following the procedure reported in [17]. The cylindrical phantom was 17 cm long and 22 cm in diameter for an inner volume of 6862 mL (Figure 2a, Table 1). A total activity of 205.9 MBq was injected in the volume, thereby obtaining a final activity concentration of 0.030 MBq/mL.
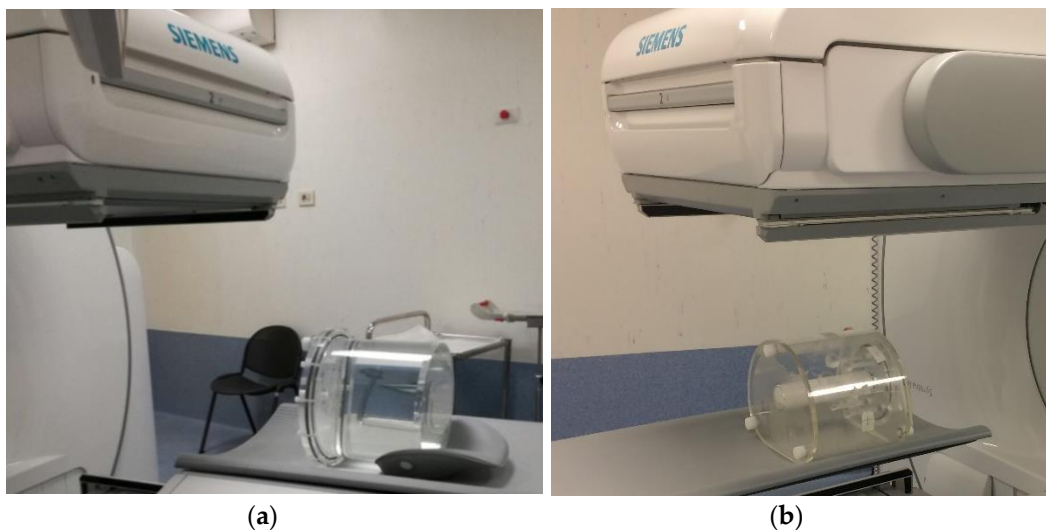

(**a**)   (**b**)

Figure 2. Data acquisition using the reference phantoms (**a**) homogeneous cylindrical and (**b**) the NEMA/IEC phantom.

Raw SPECT data for the reference cylindrical phantom were reconstructed testing two methods (Table 2) using a 256 × 256 matrix with 2.39 mm^3 voxel size as described in the following.

Table 2. Raw SPECT data for the reference cylindrical phantom were reconstructed using both the Symbia Intevo SPECT/CT built-in software.

Software	Algorithm	Parameters
xSPECT	OSEM	8 iterations, 4 subsets, no filters
	OSCG	24 iterations, 2 subsets, 2.5 mm Gaussian filter

The first investigated method was the well-known Ordered Subset Expectation Maximization technique (OSEM, 8 iterations, 4 subsets, no filters) that provides images expressed in counts. The second method was the novel xSPECT reconstruction algorithm based on the Ordered Subset Conjugated Gradient method (OSCG, 24 iterations, 2 subsets, 2.5 mm Gaussian filter) that provides images directly expressed in units of Bq/mL without the need a post-reconstruction scaling of voxels values to quantitative values [20]. In xSPECT software, attenuation correction is achieved generating μ-maps from CT data, converting Hounsfield units to μ values using a bi-linear transformation. Scatter correction is performed by using the triple energy window technique [21,22].

The number of iterations and subsets used for OSEM reconstruction (8 and 4, respectively) was selected based on standard protocols adopted in the clinical practice.

Similarly, the number of iterations and subsets used with OSCG in association with post-smoothing (i.e., 24 iterations, 2 subsets, 2.5 mm Gaussian filter) was selected based on a preliminary internal study investigating the best combination in the range of 1–7 subsets and 1–30 iterations. Of note, our results confirmed the manufacturer recommendations.

A comparison was performed between profiles generated at a central slice of the phantom reconstructed with the xSPECT software, in order to investigate the relative differences of the activity profiles.

At present, there is no general agreement on the best method to outline a given region of interest (ROI) in emission tomography. The size of the selected region may have a significant impact on the final activity recovered in the imaged phantom, especially in the presence of small objects and in areas close to the phantom wall. Consequently, we decided to compare three different ROI delineation methods: a cylindrical ROI representing the cylindrical phantom's physical inner volume (ROI1) was firstly generated, from which a second and a third ROIs were obtained using an automatic contraction to include the 80% of the phantom's volume (ROI2) and a third ROI including the external wall of the phantom (ROI3) using the automatic whole-body tool. For each defined ROI, the recovery coefficient (RC) and the coefficient of variation (*COV*) were also determined as follows:

- Recovery coefficient in a uniform geometry (**RC_{ug}**):

$$RC_{ug} = \frac{c_{bg}}{C_{bg}} \tag{2}$$

with c_{bg} the activity concentration measured in the reconstructed SPECT phantom background and C_{bg} the expected activity concentration known from the phantom preparation. c_{bg} was evaluated as the average the 3 concentric cylindrical ROIs centered on the cylinder axis placed at different locations using the MIM workstation (MIM Software Inc., Cleveland, OH, USA).

- The **COV**, representative of the image noise was evaluated according to the following formula [17]:

$$COV = \frac{\sigma_{bg}}{c_{bg}} \times 100 \tag{3}$$

where σ_{bg} is the standard deviation of the activity concentration in each slice.

Finally, activity volume histograms (AVHs) were determined in order to assess possible heterogeneity areas within the ROIs.

The best reconstruction approach to be used in the reconstruction of the NEMA/IEC phantom and the 3D-printed phantom was selected according to the best agreement between measured and expected activity.

2.3. Determinations of Recovery Coefficients Using the NEMA/IEC Phantom

A NEMA/IEC NU2 (Figure 2b, Table 2) phantom was then used to assess the recovery coefficient (RC_j) in spherical objects as a function of the sphere size. Six spherical inserts of 10, 13, 17, 22, 28, and 37 mm diameter were filled with an activity concentration (C_{sph}) of 1.74 MBq/mL in a cold background. For each spherical insert ($j = 1 \dots 6$) the RC_j were defined by four different ROI delineation methods according to the following equations:

$$RC_{j,max} = \frac{c_{sph,j,max}}{C_{sph}}$$

$$RC_{j,50\%} = \frac{c_{sph,j,50\%}}{C_{sph}}$$

$$RC_{j,PE} = \frac{c_{sph,j,PE}}{C_{sph}}$$

$$RC_{j,V} = \frac{c_{sph,j,V}}{C_{sph}} \tag{4}$$

where:

- $c_{sph,j,max}$ is the measured maximum voxel value (in terms of activity concentration) for a given spherical insert ($j = 1$ to 6);
- $c_{sph,j,50\%}$ is the average voxel value for each hot insert volume of interest (VOI) defined by a 3D iso-contour at 50% adapted for background as recommended by the EANM Guidelines for FDG tumor PET imaging [23].
- $c_{sph,j,PE}$ is the average voxel values for each hot insert VOI assessed with the PET-Edge (PE) tool, a gradient-based technique that detects the steepest drop off in SUV values to create the contour boundary automatically.
- $c_{sph,j,V}$ is the average voxel values for each VOI corresponding to the physical volume of each sphere. In this work we used a semi-automatic segmentation method to obtain 3D spherical contours (2D/3D brush tool) adopting the physical diameter of the inserts

2.4. Workflow Validation Using Abdo-Man

The method was validated in non-reference geometry using a 3D-printed anthropomorphic phantom provided with a liver section with multiple inserts for lesion representation [15].

The phantom is designed using the anatomical information of a 32-year-old male volunteer with an appropriate liver volume to simulate patients undergoing RE. Liver volume was obtained from MRI data and 3D printing technique. Anatomical data were obtained by Gear et al. [15] from MRI data using a Siemens Aera 1.5 T MRI scanner. The required organ volumes were generated from the anatomical dataset and then delineated and segmented on the Hermes Hybrid Viewer 2.2c image processing software (Stockholm, Sweden) to create a new dataset containing only the required outlined volumes [15]. The phantom is equipped with a fillable liver volume to produce realistic hepatic activity distributions; in addition, multiple spheres with diameters of 20, 40 and a 40 mm spherical shell (a 40 mm hollow sphere containing an inner sphere with 25 mm diameter), 1 mm wall thicknesses and detachable supports to connect them to the liver base can be placed inside the main liver volume to simulate a lesion of different size and heterogeneity.

The phantom was manufactured using a Stratasys Connex3 PolyJet 3D printer using solid acrylic plastic, with similar properties to polymethylmethacrylate (PMMA). Lesion inserts were printed using a transparent polymer, (VeroClear FullCure 810). Once assembled, the liver void can be filled via an access port in the base of the phantom.

Schematic images of the phantom's design and inserts are shown in Figure 3. Data acquisition was performed using a total of 183 MBq of ^{99m}Tc for the liver compartment (0.102 MBq/mL) while the lesion inserts were filled with a ^{99m}Tc activity concentration of 0.510 MBq/mL to give a final liver-to-lesion concentration ratio of 1:5, approximately.
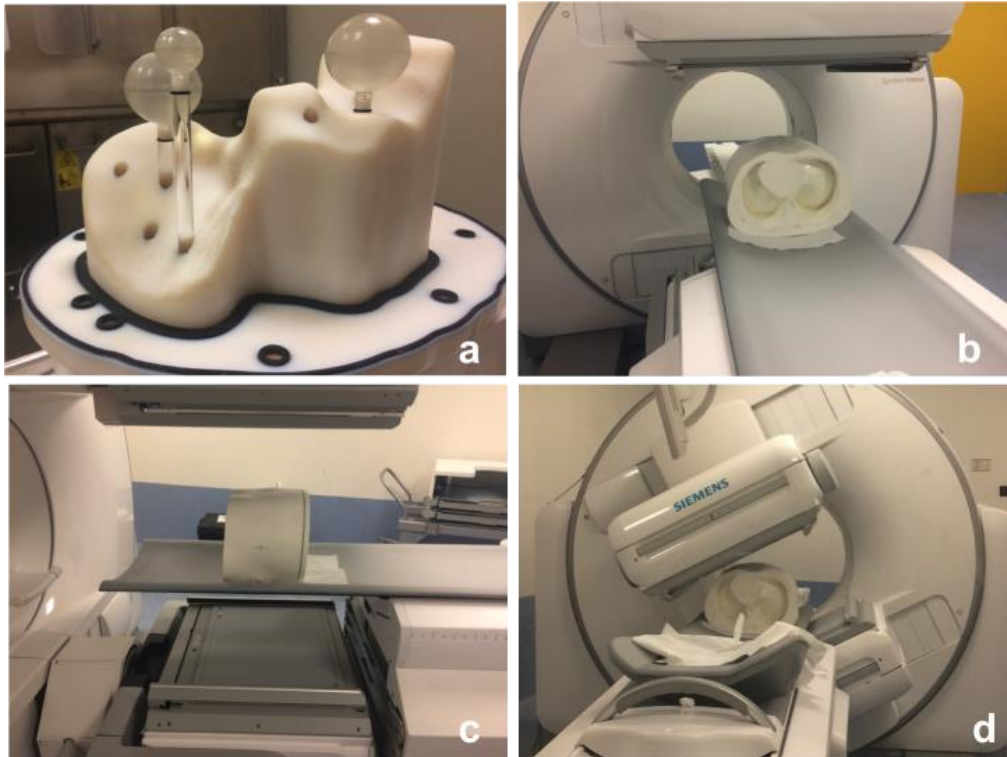

Figure 3. (**a**) The Abdo-Man phantom's design and schematic illustration indicating how lesion and support rods are placed within the phantom; (**b**,**c**) the position of phantom on the couch; (**d**) a step of SPECT acquisition.

ROIs corresponding to the total volume of the phantom, the liver section volume, the three spheres' and supports physical volumes as well as the 1 cm expansions of all the above-mentioned contours were delineated for the Abdo-Man phantom.

All the above-mentioned ROIs and AVHs were obtained using MIM 6.1.7 workstation with the semi-automatic segmentation method 2D/3D brush tool adopting the physical diameter of the inserts. Figure 4 shows the transaxial and coronal cross section of all the used phantoms as obtained by MIM software.
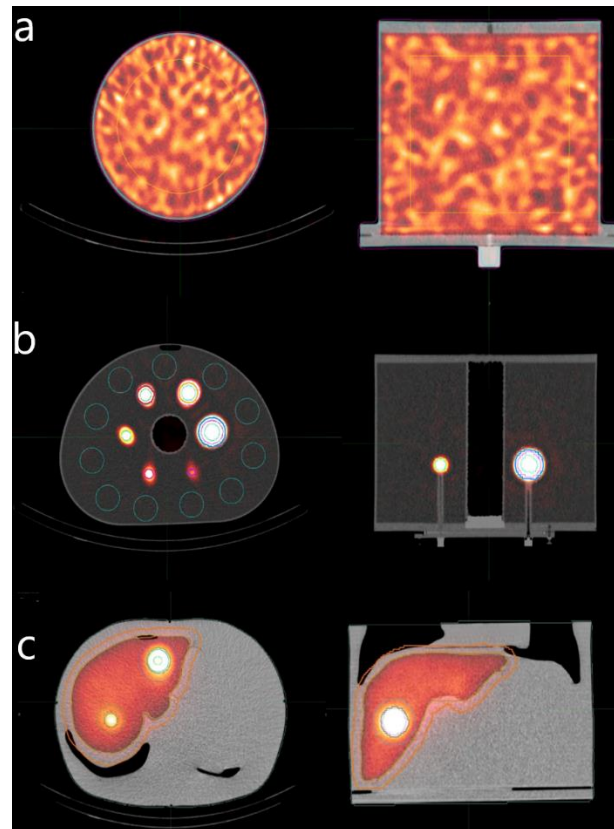
Figure 4. A transaxial and coronal cross-section of the used phantoms: (**a**) cylindrical phantom, (**b**) NEMA/IEC NU2 phantom, and (**c**) Abdo-Man anthropomorphic phantom.

3. Results

3.1. Point Source

Figure 5 shows planar images of the ^{57}Co point source. The experimental difference between nominal and measured average activity resulted to be within 3%, in good agreement with the manufacturer indications.

Figure 5. Planar images obtained from the system calibration with the ^{57}Co point source.

3.2. Homogeneous Cylindrical Phantom

Examples of data reconstructed with (a) OSCG and (b) OSEM algorithm in xSPECT software for the homogeneous phantom are shown in Figure 6.
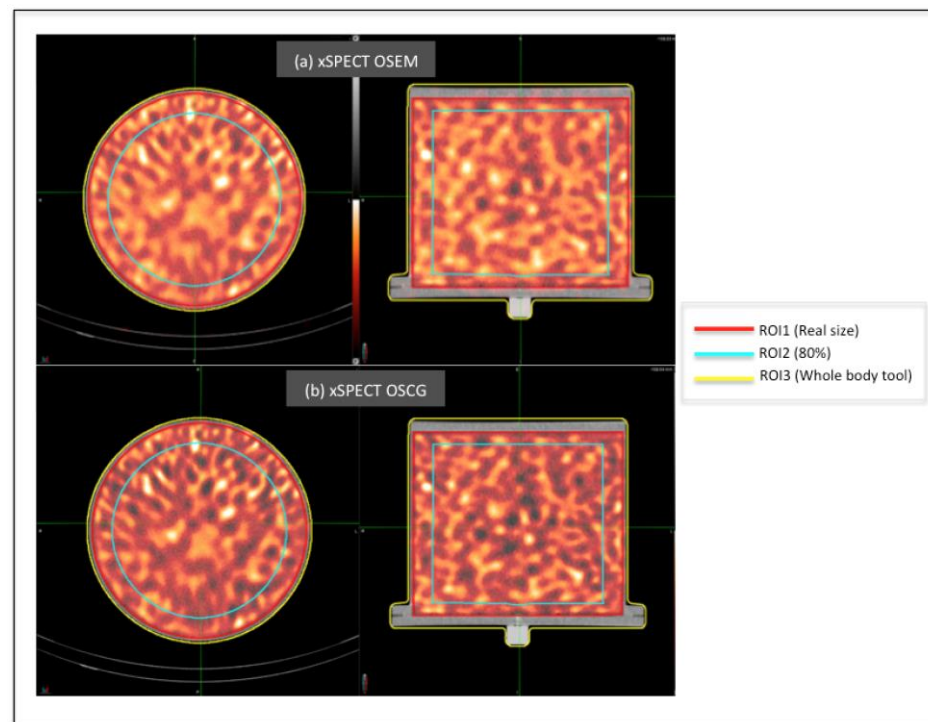
Figure 6. Data reconstructed with (**a**) OSEM and (**b**) OSCG algorithm in xSPECT system for the homogeneous phantom.

For the homogeneous phantom, the nominal (C_{bg}) and measured (c_{bg}) activity concentration in the phantom background at the time of the acquisition, the standard deviation of the activity concentration values (σ_{bg}) the recovery coefficient (RC_{ug}) and the coefficient of variation (COV) are reported in Table 3. The first two delineation methods (ROI1 and ROI2) provided an excellent agreement with the know activity concentration with a recovery coefficient (RC_{ug}) of 1.00 and 1.02, respectively. As expected, the third delineation method (ROI3) resulted in a lower RC_{ug}, as the expansion of the ROI out of the physical volume provided lower activity values. It is worth noting that all three methods provided activity concentration values consistent with the accuracy stated by the manufacture (below 10%).

Table 3. Calibration factors assessed for the homogeneous phantom. C_{bg} represents the known activity concentration in the phantom, c_{bg} is the measured activity, σ_{bg} is the standard deviation of the activity concentration values, RC_{ug} is the recovery coefficient of the cylindrical phantom and COV is the coefficient of variation.

ROIs	C_{bg} (MBq/mL)	c_{bg} (MBq/mL)	σ_{bg} (MBq/mL)	RC_{ug}	COV (%)
ROI 1	0.030 ($\pm$5%)	0.0301	0.007	1.00	23%
ROI 2	0.030 ($\pm$5%)	0.0305	0.007	1.02	22%
ROI 3	0.030 ($\pm$5%)	0.0278	0.010	0.93	36%

Figure 7 compares activity concentration profiles obtained using different reconstruction algorithms. No substantial differences are reported between xSPECT with OSCG or OSEM when images are normalized to their maximum values, confirming that OSEM and OSCG differ only for a counts-to-Bq/mL rescaling factor. Therefore, xSPECT with the OSCG algorithm was used for image reconstruction in the NEMA phantom and in the 3D printed phantom.
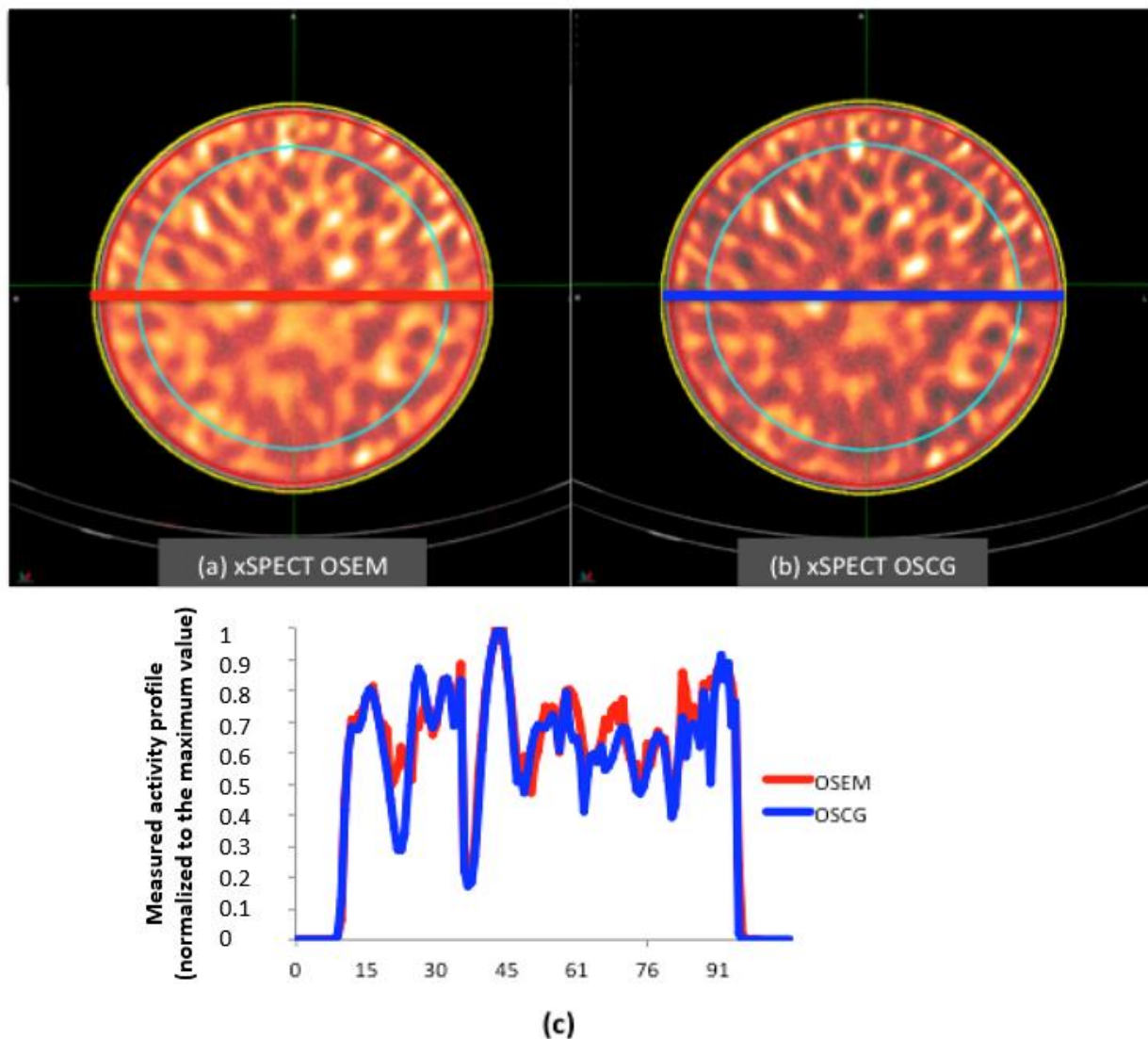
Figure 7. (**a**) Profiles generated at a central slice of the homogeneous phantom reconstructed with the xSPECT software using OSEM algorithm (blue line) with respect to (**b**) OSCG algorithm (red line); (**c**) Activity profiles.

The analysis of AVHs of the homogeneous phantom for the three ROIs is reported in Figure 8. The activity concentration obtained considering the physical volume of the homogeneous phantom (blue line) clearly underestimates the known activity value in the phantom due to spill out effects. Activity underestimations are exacerbated when the phantom wall and cap are included in the ROI (ROI3, green line). Spill out effects are shown in Figure 7c, with activity concentration suddenly decreasing close to the phantom walls. ROI2, including 80% of the phantom's volume, provided the best results with an agreement below 2% between measured activity concentration and known activity concentration value.
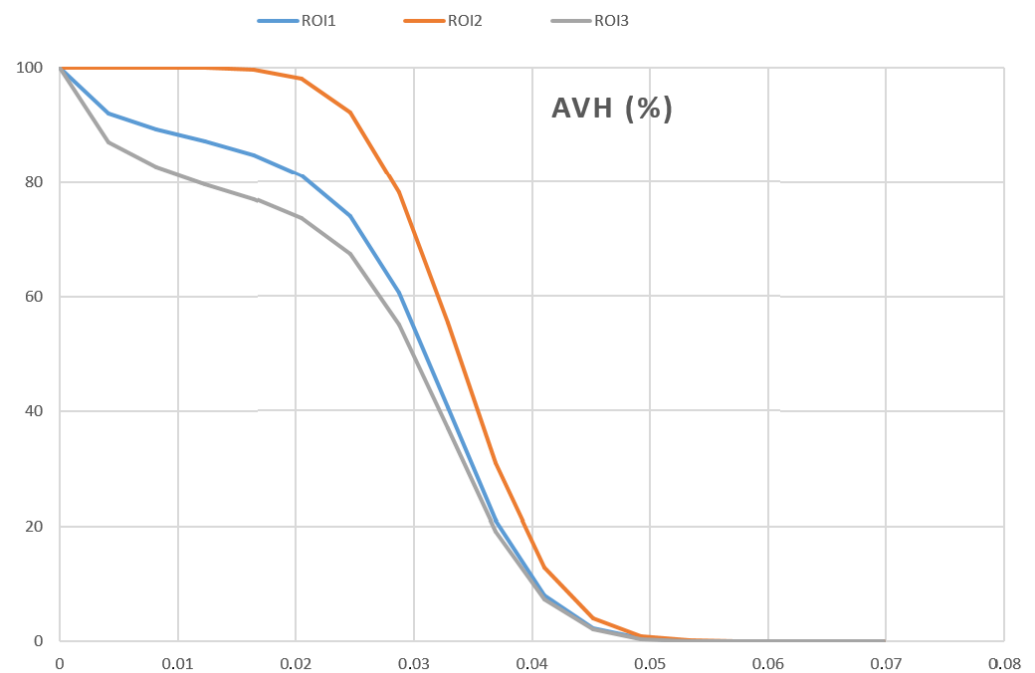
Figure 8. AVHs of three ROIs delineated on cylindrical homogenous phantom are reported. ROI1 = delineation performed considering the physical volume of the phantom. ROI2 = delineation performed considering 80% of the inner volume of the cylinder. ROI3 = delineation performed with the Whole Body Tool to include phantom wall and cap.

3.3. NEMA/IEC Phantom

Signal recovery RCj measured in spherical inserts of the NEMA/IEC phantom are reported in Figure 9. The results obtained for RCj prove that the max-values method is the most accurate. However, in the present study and in the clinical practice, the physical-volume method value was established as reference method for activity correction due to its reproducibility.
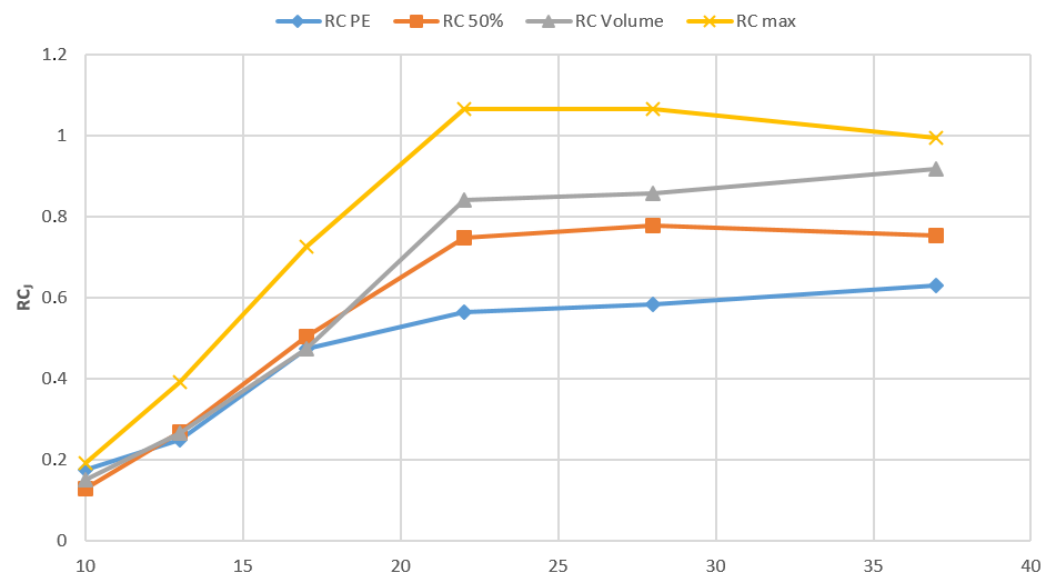

Figure 9. Recovery Coefficient (RC) as a function of the insert diameter for the NEMA/IEC phantom using different segmentation methods.

The AVHs of NEMA/IEC phantom for the 6 ROIs obtained by segmentation of the physical volume of each spherical insert are reported in Figure 10. The spill-in and spill-out phenomena are comparable for spherical insert of diameter larger than or equal to 22 mm.
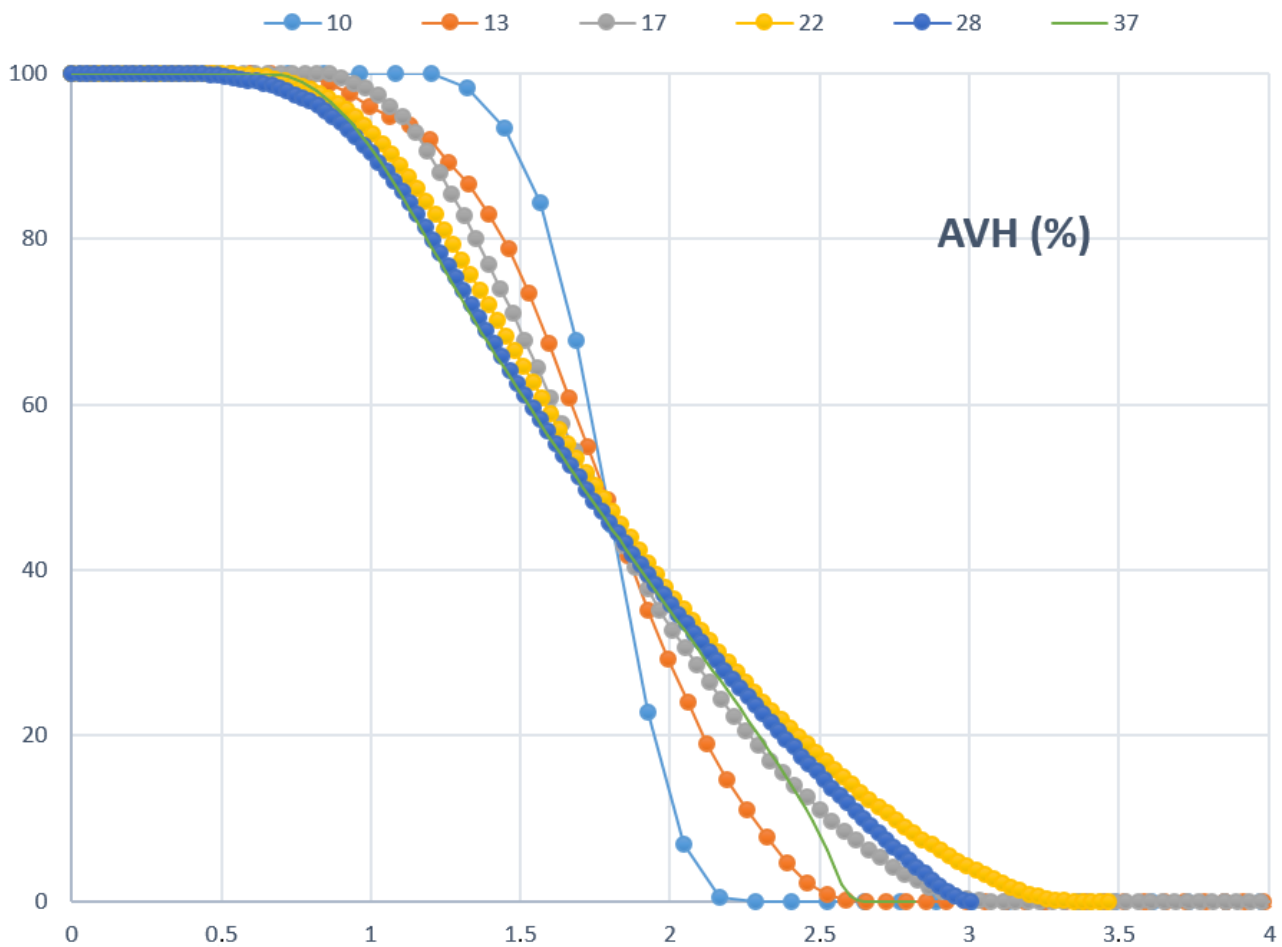

Figure 10. AVHs of three ROIs delineated on the NEMA/IEC phantom are shown against the activity concentration for the 6 investigated spheres according to the sphere diameter (in mm) taking into consideration the RCs reported in Figure 9.

3.4. Abdo-Man Phantom

The RC_{ug} and RC_j factors were used as correction factors to obtain the corrected values in MBq/mL within ROIs in the Abdo-Man phantom (Table 4). The AVHs obtained for ROIs delineated on Abdo-Man phantom and corrected using the RC_j are reported in Figure 11.

Table 4. Recovered activities for the liver and the three spherical lesions in the Abdo-Man phantom.

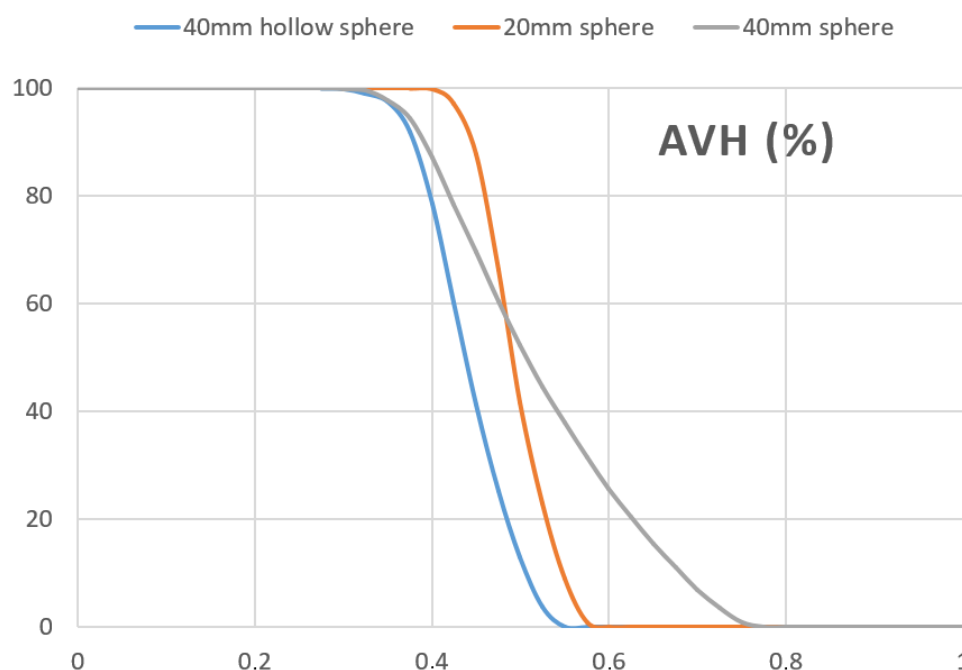| ID	Abdo-Man	C_{exp} (MBq/mL)	c_m (MBq/mL)	Δ (%)
Liver	Liver	0.103 (±5%)	0.104	+1.17%
S40	40 mm sphere	0.517 (±5%)	0.509	−1.51%
S20	20 mm sphere	0.517 (±5%)	0.537	+3.87%
S9	40 mm hollow sphere	0.517 (±5%)	0.387	−25.18%

Figure 11. AVHs of ROIs delineated on Abdo-Man phantom corrected using the RC_j reported in Figure 9.

4. Discussion

Radioembolization with ^{90}Y-loaded microspheres is increasingly used in radiation therapy for the treatment of HCC and metastatic liver lesions. The treatment requires accurate activity planning and dose determination to ensure a good therapeutic response with as few side effects as possible. At present, ^{99m}Tc-MAA imaging is largely used as a surrogate of microsphere distribution to assess potential extra-hepatic shunts as well as to estimate the absorbed doses and to personalize the activity to be administered. This procedure enables predictive patient-specific dosimetry to be performed prior to RE treatment. However, the gamma camera used for activity quantification has several inherent limitations, which restrict the spatial resolution of the images and affect the accuracy in the determination of the time-integrated activity.

Although SIRT is a well-established molecular radiotherapy approach, there are ongoing efforts to further improve treatment planning using personalised dosimetry. In fact, the general consensus is that compared with standard dosimetry, personalised dosimetry may significantly improve the response rate in patients with locally advanced hepatocellular carcinoma [24]. Personalized dosimetry can be developed using MAA-based dosimetry, which is the only evaluation available prior to ^{90}Y-loaded microspheres injection. At present, the Recent research from Levillain et al. [25] demonstrated that response of hepatic maglignancies to SIRT with resin microspheres strongly depends on tumour dose, highlighting the importance of personalized dosing regimens in SIRT therapy for improved outcome. In a recent study by Gholami [26], ^{90}Y PET/CT with pre- and post-treatment FDG PET/CT images were used to derive individual clinically relevant radiobiological parameters with the aim to evaluate the dosimetry and the treatment outcome specific to each patient. In another study by Willowson and colleagues [27] DVHs from SIRT procedures were investigated and compared to metabolic lesion response as measured with [^{18}F]FDG PET/CT to investigate the dose–response relationship for liver lesions treated with ^{90}Y resin microspheres.

Today, most literature studies addressing the issue of activity quantification in reference conditions have focused on validating the scanner geometry using simple phantoms. However, it is generally acknowledged that the validation of the quantification process on imaging phantoms based on real anatomic data has the potential to improve the quan-

titative accuracy in vivo, if optimized acquisition protocols are used. At present, few researchers have addressed the problem of quantitative accuracy using real anatomy and specific to the patient cohort of interest.

With this in mind, we tried to set-up an accurate workflow to assess the quantitative accuracy of SPECT imaging using ^{99m}Tc-MAA for target liver lesions combining cutting edge imaging technology with a 3D-printed multi-compartimental anthropomorphic phantom.

Preliminary investigations on Abdo-Man anthropomorphic phantom have been conducted using a SPECT/CT Symbia T2 without the xSPECT tool by Gear et al. [15]. The authors reported that SPECT overestimates normal liver activity (+11%, approximately) and underestimates the activity in the lesions (−11% for the 40-mm lesion, −12% for the 40-mm shell lesion and the 20-mm lesion, approximately). In their study, the authors put forward the idea that Abdo-Man should be validated using alternative reconstruction algorithms, such as the Siemens X-SPECT and Hermes SUV-SPECT software [15].

Against this backdrop in this work the SPECT/CT Symbia Intevo system provided with xSPECT quantitative software was used to assess the accuracy in quantification procedure. A number of conclusions can be drawn from the present study and are summarized in the following subsections.

4.1. Homogeneous Cylindrical Phantom

As expected, ROI delineation considering 80% of the physical volume of the cylindrical phantom provided the best activity concentration estimate (deviation below 2%). This delineation method has the potential to exclude spill out of activity from the uniform phantom. Image noise on the same phantom was assessed in terms of coefficient of variation, i.e., the ratio of the standard deviation of the activity values to the mean activity value. We found COVs in the range 23–36%, in keeping with Gensin et al. [17] reporting COV values from 12 to 38% for the homogenous phantom. This finding suggests that image noise is intrinsically high and longer acquisition times should be preferred when possible.

Concerning the image reconstruction method, xSPECT software using both OSCG and OSEM algorithm resulted to be equivalent when normalized to their maximum values. Our results suggest that xSPECT modality still presents wide margins of improvement since attenuation and scatter corrections performed by this software may introduce some artifacts in the activity distribution within hollow objects.

4.2. NEMA/IEC Phantom

As a general rule, the recovery coefficients for the 6 hot inserts of the NEMA phantom were comparable to PET-derived reference levels reported in the EANM guidelines [23].

The RC_{js} strongly depend on ROI delineation method that must be taken into consideration for performing the correction in clinical cases. The poorer RC_j was obtained using PE method while the higher RC_j was obtained using the max method.

The reference method selected in this work for activity correction factors assessment was the physical-volume method due to its reproducibility based on CT images. In addition, this method is currently adopted within our institute for liver lesion delineation in the clinical practice [28].

4.3. AbdoMan Phantom

Finally, the accuracy of the quantification was assessed by comparing the measured activity in the liver lesions and in the liver compartment with the known activity within the phantom measured at preparation. As a general rule, our quantification procedure provided excellent results for the liver compartment, where the measured activity overestimates the expected activity by +1%. Similar results were obtained for the liver lesions where the measured activity was slightly underestimated in the 40 mm sphere (−2%) and overestimated in the 20 mm sphere (+4%). The poorest result was obtained for the 40 mm hollow sphere, with an underestimation of −20% in the measured activity. This underestimation can be explained in part by imperfect correction for partial volume effects, representing a

major correction factor in very small objects. From a clinical point of view, this issue is of particular relevance for wide HCC lesions with hypoxic necrotic core, for which SPECT system may not be able to estimate the activity gradient in the circular corona. Apart from this slight discrepancy, our results compare well with those obtained by Gear et al. [15] and confirm that the SPECT/CT Symbia Intevo system along with the xSPECT software is likely to provide excellent activity estimates. Data on the quantitative accuracy are detailed in Table 4. In particular, the most striking result to emerge from this study is that the proposed acquisition protocol is capable of recovering the activity concentration even in very small objects (+4% in the 20 mm sphere).

The present findings might have important implications for dosimetry studies in RE, where accurate activity quantification in small lesions is essential to obtain reliable dose estimates. Further work needs to be done to assess the capability of modern SPECT systems and up-to-date reconstruction software to estimate the absorbed dose in 3D printed anthropomorphic phantoms. In addition, it is a question of future research to investigate the use of 3D printed phantoms provided with real clinical data (e.g., physical model of the patient's tumor), with the possibility of including personalized radiobiological parameters in the dose assessment model.

4.4. Limitations of the Study

The results reported herein should be considered in the light of some limitations. The first is that despite the 3D printed technology allowing for rapid, customized phantom fabrication for dosimetry studies, the resulting 3D phantom is characterized by well defined geometries filled with a homogeneous distribution of radioactivity, a clinical situation hardly met in patient study. Furthermore, 3D printed small objects suffer to a greater extent than larger objects from the effects of inactive walls, and therefore the recovery of activity in small objects should be interpreted with caution. Of note, recent studies explored the feasibility of realizing a 3D printed radioactive phantoms for nuclear medicine imaging, where radioactivity is incorporated into the building materials, thereby avoiding inactive walls [29,30].

5. Conclusions

Taken together, our findings add to a growing body of literature on activity quantification in liver radioembolization using ^{99m}Tc-MAA as a surrogate of microspheres. Our results demonstrate that the Symbia Intevo SPECT system, together with xSPECT software, permit an absolute quantification in anthropomorphic geometry largely within the 10% recommended from the manufacturer. Most importantly, the activity concentration in very small objects (below 40 mm diameter) can be recovered with deviations below 4%. Caution is advised in the presence of spherical objects with a necrotic core, as underestimations in the order of 20% were obtained.

Author Contributions: Conceptualization, S.U. and L.S.; methodology, S.U. and S.N.; validation, S.U. and V.B.; software, S.U. and B.C.; formal analysis, S.U. and M.D. (Marco D'Andrea); investigation, S.U and E.I.; resources, S.U., A.S. and L.S.; data curation, S.U. and B.C.; writing—original draft preparation, S.U. and L.S.; writing—review and editing, S.U., E.M., R.M., M.D. (Marco D'Arienzo), A.G. and L.S.; supervision, S.U., A.S. and L.S.; funding acquisition, S.U. and L.S. All authors have read and agreed to the published version of the manuscript.

Institutional Review Board Statement: Not applicable.

Informed Consent Statement: Not applicable.

Data Availability Statement: The data used to support the findings of this study are included within the article. Details are available from the corresponding author upon request.

Conflicts of Interest: The authors declare no conflict of interest.

Abbreviations

RE	Radioembolization
SPECT	Single Photon Emission Computed Tomography
CT	Computed Tomography
OSEM	Ordered Subset Expectation–Maximization
OSCG	Ordered Subset Conjugated Gradient
ROI	Region of Interest
PET	Positron Emission Tomography
HCC	Hepato Cellular Carcinoma
MAA	Macro Aggregated Albumin
NEMA	National Electrical Manufacturers Association
IEC	International Electrotechnical Commission
MIM	Medical Image Merge
DICOM	Digital Imaging and COmmunications in Medicine
AAPM	American Association of Physicists in Medicine
MIRD	Medical Internal Radiation Dose
SUV	Standardized Uptake Value
2D	Two Dimension
3D	Three Dimension
LEHR	Low-Energy High-Resolution
NIST	National Institute of Standards and Technology
EANM	European Association of Nuclear Medicine
FDG	Fluoro-Deoxy-Glucose
VOI	Volume of Interest
MRI	Magnetic Resonance Imaging
PMMA	Poly Methyl Metha Acrylate
AVHs	Activity Volume Histograms

References

1. Sung, H.; Ferlay, J.; Siegel, R.; Laversanne, M.; Soerjomataram, I.; Jemal, A.; Bray, F. Global Cancer Statistics 2020: GLOBOCAN Estimates of Incidence and Mortality Worldwide for 36 Cancers in 185 Countries. *CA Cancer J. Clin.* **2021**, *71*, 209–249. [CrossRef]
2. Wong, M.; Jiang, J.; Goggins, W.; Liang, M.; Fang, Y.; Fung, F.; Leung, C.; Wang, H.; Wong, G.; Wong, V.; et al. International incidence and mortality trends of liver cancer: A global profile. *Sci. Rep.* **2017**, *7*, 45846. [CrossRef]
3. Soerjomataram, I.; Lortet-Tieulent, J.; Parkin, D.; Ferlay, J.; Mathers, C.; Forman, D.; Bray, F. Global burden of cancer in 2008: A systematic analysis of disability-adjusted life-years in 12 world regions. *Lancet* **2012**, *380*, 1840–1850. [CrossRef]
4. Altekruse, S.; McGlynn, K.; Reichman, M. Hepatocellular Carcinoma Incidence, Mortality, and Survival Trends in the United States From 1975 to 2005. *J. Clin. Oncol.* **2009**, *27*, 1485–1491. [CrossRef]
5. Khan, S.; Davidson, B.; Goldin, R.; Heaton, N.; Karani, J.; Pereira, S.; Rosenberg, W.; Tait, P.; Taylor-Robinson, S.; Thillainayagam, A.; et al. Guidelines for the diagnosis and treatment of cholangiocarcinoma: An update. *Gut* **2012**, *61*, 1657–1669. [CrossRef]
6. Kennedy, A.; Nutting, C.; Coldwell, D.; Gaiser, J.; Drachenberg, C. Pathologic response and microdosimetry of 90Y microspheres in man: Review of four explanted whole livers. *Int. J. Radiat. Oncol. Biol. Phys.* **2004**, *60*, 1552–1563. [CrossRef]
7. Sato, K.; Lewandowski, R.; Bui, J.; Omary, R.; Hunter, R.; Kulik, L.; Mulcahy, M.; Liu, D.; Chrisman, H.; Resnick, S.; et al. Treatment of Unresectable Primary and Metastatic Liver Cancer with Yttrium-90 Microspheres (TheraSphere®): Assessment of Hepatic Arterial Embolization. *CardioVascular Interv. Radiol.* **2006**, *29*, 522–529. [CrossRef]
8. Srinivas, S.; Shrikanthan, S.; Yu, N.; Kost, S.; Gurajala, R.; Karuppasamy, K. Treatment planning part II: Procedure simulation and prognostication. In *Handbook of Radioembolization: Physics, Biology, Nuclear Medicine, and Imaging*; Pasciak, A., McKinney, J., Bradley, Y., Eds.; CRC Press/Taylor & Francis: Boca Raton, FL, USA, 2017.
9. Gulec, S.; Mesoloras, G.; Stabin, M. Dosimetric techniques in 90Y-microsphere therapy of liver cancer: The MIRD equations for dose calculations. *J. Nucl. Med.* **2006**, *47*, 1209–1211.
10. Ho, S.; Lau, W.; Leung, T.; Chan, M.; Ngar, Y.; Johnson, P.; Li, A. Partition model for estimating radiation doses from yttrium-90 microspheres in treating hepatic tumours. *Eur. J. Nucl. Med.* **1996**, *23*, 947–952. [CrossRef]

11. Pasciak, A.; Bourgeois, A.; Bradley, Y. A Comparison of Techniques for 90Y PET/CT Image-Based Dosimetry Following Radioembolization with Resin Microspheres. *Front. Oncol.* **2014**, *4*, 121. [CrossRef]

12. D'Arienzo, M.; Pimpinella, M.; Capogni, M.; De Coste, V.; Filippi, L.; Spezi, E.; Patterson, N.; Mariotti, F.; Ferrari, P.; Chiaramida, P.; et al. Phantom validation of quantitative Y-90 PET/CT-based dosimetry in liver radioembolization. *EJNMMI Res.* **2017**, *7*, 94. [CrossRef]

13. Kao, Y.; Hock Tan, A.; Burgmans, M.; Irani, F.; Khoo, L.; Gong Lo, R.; Tay, K.; Tan, B.; Hoe Chow, P.; Eng Ng, D.; et al. Image-Guided Personalized Predictive Dosimetry by Artery-Specific SPECT/CT Partition Modeling for Safe and Effective ^{90}Y Radioembolization. *J. Nucl. Med.* **2012**, *53*, 559–566. [CrossRef]

14. Garin, E.; Rolland, Y.; Lenoir, L.; Pracht, M.; Mesbah, H.; Porée, P.; Laffont, S.; Clement, B.; Raoul, J.; Boucher, E. Utility of Quantitative 99mTc-MAA SPECT/CT for 90yttrium-Labelled Microsphere Treatment Planning: Calculating Vascularized Hepatic Volume and Dosimetric Approach. *Int. J. Mol. Imaging* **2011**, 398051. [CrossRef]

15. Gear, J.; Cummings, C.; Craig, A.; Divoli, A.; Long, C.; Tapner, M.; Flux, G. Abdo-Man: A 3D-printed anthropomorphic phantom for validating quantitative SIRT. *EJNMMI Phys.* **2016**, *3*, 17. [CrossRef]

16. D'Arienzo, M.; Cazzato, M.; Cozzella, M.; Cox, M.; D'Andrea, M.; Fazio, A.; Fenwick, A.; Iaccarino, G.; Johansson, L.; Strigari, L.; et al. Gamma camera calibration and validation for quantitative SPECT imaging with ^{177}Lu. *Appl. Radiat. Isot.* **2016**, *112*, 156–164. [CrossRef]

17. Gnesin, S.; Leite Ferreira, P.; Malterre, J.; Laub, P.; Prior, J.; Verdun, F. Phantom Validation of Tc-99m Absolute Quantification in a SPECT/CT Commercial Device. *Comput. Math. Methods Med.* **2016**, 4360371. [CrossRef]

18. American Association of Physicists in Medicine. *The Selection, Use, Calibration, and Quality Assurance of Radionuclide Calibrators Used in Nuclear Medicine*; Report of AAPM Task Group 181; AAPM: College Park, MD, USA, 2012.

19. Zhao, W.; Esquinas, P.; Hou, X.; Uribe, C.; Gonzalez, M.; Beauregard, J.; Dewaraja, Y.; Celler, A. Determination of gamma camera calibration factors for quantitation of therapeutic radioisotopes. *EJNMMI Phys.* **2018**, *5*, 8.

20. Armstrong, I.; Hoffmann, S. Activity concentration measurements using a conjugate gradient (Siemens xSPECT) reconstruction algorithm in SPECT/CT. *Nucl. Med. Commun.* **2016**, *37*, 1212–1217. [CrossRef]

21. D'Arienzo, M.; Cozzella, M.; Fazio, A.; Cazzato, M.; Ungania, S.; Iaccarino, G.; D'Andrea, M.; Schmidt, K.; Kimiaei, S.; Strigari, L. Quantitative 177Lu SPECT imaging using advanced correction algorithms in non-reference geometry. *Phys. Med.* **2016**, *32*, 1745–1752. [CrossRef]

22. Iida, H.; Eberl, S.; Kim, K.; Tamura, Y.; Ono, Y.; Nakazawa, M.; Sohlberg, A.; Zeniya, T.; Hayashi, T.; Watabe, H. Absolute quantitation of myocardial blood flow with 201Tl and dynamic SPECT in canine: Optimisation and validation of kinetic modelling. *Eur. J. Nucl. Med. Mol. Imaging* **2008**, *35*, 896–905. [CrossRef]

23. Boellaard, R.; Delgado-Bolton, R.; Oyen, W.; Giammarile, F.; Tatsch, K.; Eschner, W.; Verzijlbergen, F.; Barrington, S.; Pike, L.; Weber, W.; et al. FDG PET/CT: EANM procedure guidelines for tumour imaging: Version 2.0. *Eur. J. Nucl. Med. Mol. Imaging* **2014**, *42*, 328–354. [CrossRef] [PubMed]

24. Garin, E.; Tselikas, L.; Guiu, B.; Chalaye, J.; Edeline, J.; de Baere, T.; Assenat, E.; Tacher, V.; Robert, C.; Terroir-Cassou-Mounat, M.; et al. Personalised versus standard dosimetry approach of selective internal radiation therapy in patients with locally advanced hepatocellular carcinoma (DOSISPHERE-01): A randomised, multicentre, open-label phase 2 trial. *Lancet Gastroenterol. Hepatol.* **2021**, *6*, 17–29. [CrossRef]

25. Levillain, H.; Duran Derijckere, I.; Ameye, L.; Guiot, T.; Braat, A.; Meyer, C.; Vanderlinden, B.; Reynaert, N.; Hendlisz, A.; Lam, M.; et al. Personalised radioembolization improves outcomes in refractory intra-hepatic cholangiocarcinoma: A multicenter study. *Eur. J. Nucl. Med. Mol. Imaging* **2019**, *46*, 2270–2279. [CrossRef]

26. Gholami, Y.; Willowson, K.; Bailey, D. Towards personalised dosimetry in patients with liver malignancy treated with ^{90}Y-SIRT using in vivo-driven radiobiological parameters. *EJNMMI Phys.* **2022**, *9*, 49. [CrossRef] [PubMed]

27. Willowson, K.; Eslick, E.; Bailey, D. Individualised dosimetry and safety of SIRT for intrahepatic cholangiocarcinoma. *EJNMMI Phys.* **2021**, *8*, 65. [CrossRef] [PubMed]

28. Sciuto, R.; Rea, S.; Pizzi, G.; Vallati, G.E.; Strigari, L. Radioembolization of Hepatic Metastases with 90Y-Microspheres: Indications and Procedure. In *Clinical Applications of Nuclear Medicine Targeted Therapy*; Bombardieri, E., Seregni, E., Evangelista, L., Chiesa, C., Chiti, A., Eds.; Springer: Cham, Switzerland, 2018.

29. Läppchen, T.; Meier, L.; Fürstner, M.; Prenosil, G.; Krause, T.; Rominger, A.; Klaeser, B.; Hentschel, M. 3D printing of radioactive phantoms for nuclear medicine imaging. *EJNMMI Phys.* **2020**, *7*, 22. [CrossRef] [PubMed]

30. Gillett, D.; Marsden, D.; Ballout, S.; Attili, B.; Bird, N.; Heard, S.; Gurnell, M.; Mendichovszky, I.; Aloj, L. 3D printing 18F radioactive phantoms for PET imaging. *EJNMMI Phys.* **2021**, *8*, 38. [CrossRef]